Scripta Materialia 281 (2026) 117392

Contents lists available at ScienceDirect

Scripta Materialia

journal homepage: www.journals.elsevier.com/scripta-materialia

Thermomechanical-cycle-induced mesoscale concentric microstructural patterns in additively manufactured superalloys

Yang Wang [a,1], Zhaowei Wang [a,1], Sicong Lin [b], Zhuangzhuang Zhang [a], Lin Shi [c], Qiang Li [d,*], R. Lakshmi Narayan [e], Upadrasta Ramamurty [d,2], Kai Chen [a,*]

[a] Center for Advancing Materials Performance from the Nanoscale (CAMPNano), State Key Laboratory for Mechanical Behavior of Materials, Xi'an Jiaotong University, Xi'an 710049, China
[b] Xi'an Superalloy Technologies Co., Ltd, Xi'an 710200, China
[c] Institute of Surface-Earth System Science, School of Earth System Science, Tianjin University, Tianjin 300072, China
[d] School of Mechanical and Aerospace Engineering, Nanyang Technological University, Singapore 639798, Singapore
[e] Department of Materials Science and Engineering, Indian Institute of Technology, Delhi, New Delhi 110016, India

ARTICLE INFO

Keywords:
Ni-based superalloy
Laser directed energy deposition
Tree-ring-like microstructure
Thermal cycling

ABSTRACT

The microstructural features of additively manufactured alloys are distinct from those of their conventionally manufactured counterparts, with the combination of the alloy and the processing methods and parameters imparting uniqueness. Herein, we report one such distinct, and hitherto unreported, feature of mesoscale concentric tree-ring-like microstructure within the columnar grains in the Ni-based superalloy fabricated using the laser directed energy deposition technique. Each columnar grain comprises dendrites tens of micrometers in width. Within individual dendrite, cylindrical concentric patterns develop with radial axes perpendicular to the build direction, characterized by relatively coarsened γ' precipitates along concentric walls and finer precipitates between them, producing a tree-ring-like morphology on the laser scan plane. Elemental segregation and dislocation distributions correlate with both the dendritic framework and concentric patterns. Their formation is attributed to the coupled effects of microsegregation-induced intradendritic solvus temperature gradients and thermomechanical cycling that occurs during layerwise fabrication.

Ni-based superalloys are the materials of choice for high-temperature components in aero-engines and gas turbines, with their service performance critically governed by microscopic distributions of alloy elements, precipitates, and defects (such as dislocations and high- and low-angle grain boundaries) [1–3]. Laser directed energy deposition (L-DED) has emerged as a promising additive manufacturing (AM) technique for fabrication and repair of superalloy components with complex geometries [4–6]. The thermomechanical history, characterized by repeated heating/cooling cycles, significant heat accumulation, spatially non-uniform temperature gradients, and associated cyclic elastic-plastic deformation, intrinsic to such processing techniques often results in a highly complex microstructures in the as-built superalloys. In most AM technologies components are fabricated in a layer-wise manner, which results substantial reheating of the already-deposited layers during subsequent passes [7]. Such thermal cycling not only induces thermal stresses but may also activate dynamic recovery and recrystallization [8,9]. In comparison with other AM techniques such as laser powder bed fusion (L-PBF), L-DED operates with a larger melt pool and a lower cooling rate, leading to coarser dendritic structures and more pronounced chemical gradients from dendrite cores to interdendritic regions [10]. Whether their combined effects give rise to unique microstructures under thermomechanical cycling is yet to be ascertained [11]. In this work, we report a unique tree-ring-like concentric microstructure in L-DED-fabricated Ni-based superalloys. The pattern is characterized by the periodic distribution of γ' precipitates and dislocation densities. Similar to how tree rings record climatic history during tree growth, the concentric ring patterns serve as a microstructural record of cyclic thermomechanical exposure inherent to AM. Detailed

* Corresponding authors.
E-mail addresses: liqiangmse@gmail.com (Q. Li), kchenlbl@gmail.com (K. Chen).
[1] These authors contributed equally.
[2] Upadrasta Ramamurty was an Editor of the journal during the review period of the article. To avoid a conflict of interest, Upadrasta Ramamurty was blinded to the record and another editor processed this manuscript.

https://doi.org/10.1016/j.scriptamat.2026.117392
Received 12 February 2026; Received in revised form 9 May 2026; Accepted 14 May 2026
Available online 15 May 2026
1359-6462/© 2026 Acta Materialia Inc. Published by Elsevier Inc. All rights are reserved, including those for text and data mining, AI training, and similar technologies.

microstructural characterization is performed and the underlying formation mechanism is elucidated, providing new insights into the relationship between cyclic thermomechanical history and microstructural evolution during L-DED.

Superalloy blocks, with square cross-section of 15 mm × 15 mm and varying heights, ranging from 20 to 80 mm, were fabricated using a custom-designed L-DED system equipped with a Nd:YAG laser. The laser spot diameter, laser power, scanning velocity, and layer thickness were fixed at 3 mm, 2500 W, 30 mm/s, and 0.3 mm, respectively. Gas-atomized superalloy powders (chemical composition in weight percent: 9.3 Cr, 13.5 Co, 3.2 Mo, 1.5 W, 4.6 Ti, 5.3 Al, 0.9 Nb, 0.15 C, and balance Ni) with 45 - 106 μm in diameter were coaxially injected into the laser-induced molten pool on the surface of a stainless-steel substrate. The layer increment was set to 0.3 mm; within each layer, a bidirectional linear scanning strategy was employed, with scan tracks parallel to the X direction, as schematically illustrated in Fig. S1 of the Supplementary Information. Representative image of the as-printed blocks is shown in Fig. S2a. For clarity, a Cartesian coordinate system (O-XYZ), where the Z-direction aligns with the build direction (BD), while the X-Y plane is the deposition plane, is used. Specimens were sectioned from the as-built blocks, mechanically polished, and chemically etched using a $FeCl_3$ – HCl – H_2O solution. Microstructures were examined using optical (OM), scanning electron (SEM), and transmission electron (TEM) microscopies. Elemental and crystallographic analyses were conducted using electron probe micro-analysis (EPMA) and electron backscatter diffraction (EBSD, step size of 0.5 μm), respectively.

The as-fabricated alloy exhibits a hierarchical microstructure (Fig. 1a) characterized by [001]-oriented coarse columnar grains (average width: ~1.23 mm) that are approximately parallel to BD. These grains consist of dendrites displaying secondary arms with fourfold symmetry (Fig. 1b). In conventionally cast superalloys, the dendrites are well-developed with sharp secondary arms [12]. In the L-PBF alloys, they typically are highly underdeveloped [13]. In the present L-DED specimens, in contrast, while the secondary dendrite arms are identifiable (assisted by the discrete blocky micro-sized eutectics and carbides appearing in the interdendritic regions), they are markedly blunted [10]. This indicates a cooling rate intermediate between those of casting and L-PBF, being substantially lower than that of L-PBF despite remaining higher than that of casting [14].

This inference is further supported by the presence of well-faceted cuboidal γ' precipitates in the L-DED specimen (Fig. S2b and c), in

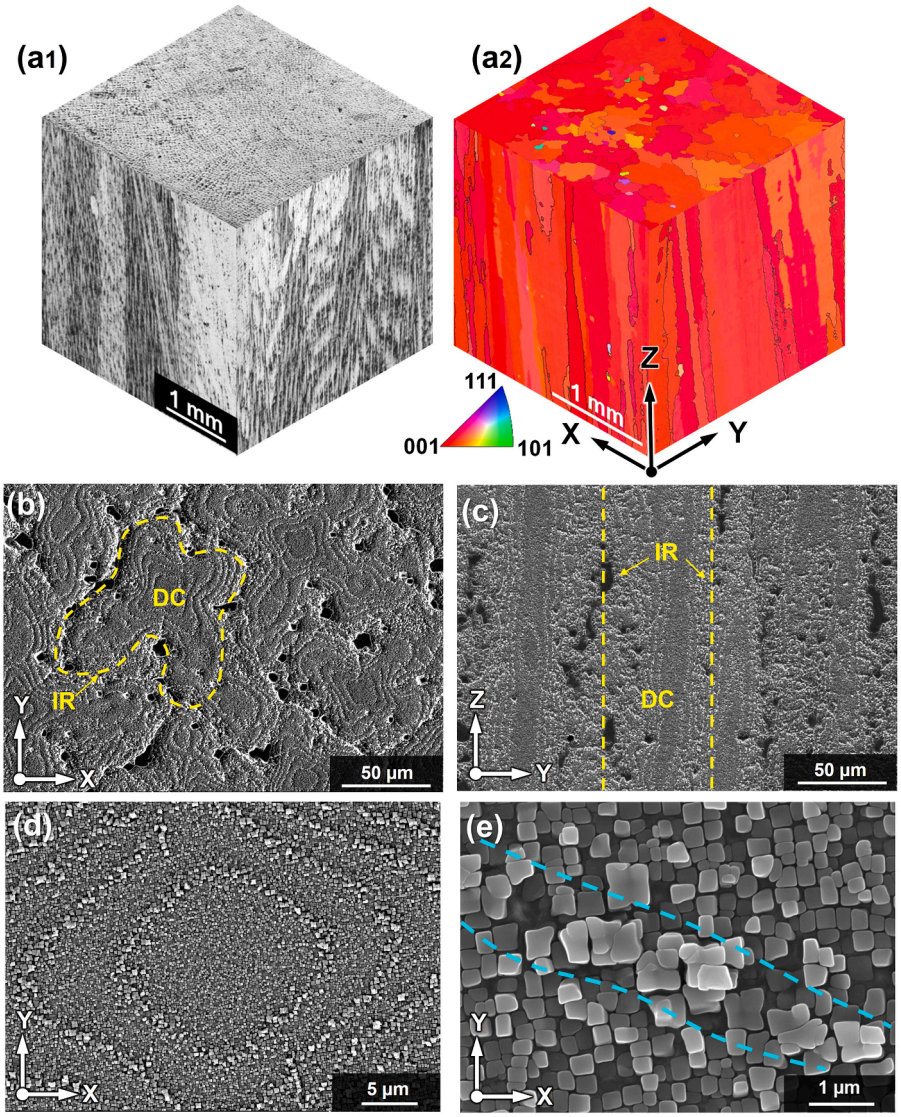


Fig. 1. (a) Representative three-dimensional microstructure: (a1) OM images, (a2) grain orientation maps with IPF-Z coloring. SEM image of (b) the dendrite structure on the XY plane, (c) the tree-ring-like microstructure on the XY plane, (d) the tree-ring-like microstructure on the YZ plane, and (e) the γ' precipitates on the XY plane.

contrast to the rounded morphology commonly reported in L-PBF superalloys [15]. In the inter-dendritic regions (IRs), the γ' precipitates exhibit a larger size (side length 414 ± 31 nm) than those within dendrite cores (299 ± 22 nm). This size disparity reflects the strong enrichment of γ'-forming elements in IRs, indicating pronounced microsegregation during solidification. From the YZ-section (Fig. 1c), the primary dendrite arm spacing is accurately determined as 59 ± 10 μm. Based on the empirical relationship: $\lambda = b\dot{T}^{-m}$, where λ is the dendrite spacing, b and m are material-specific constants (42 μm and 0.33 [16]), respectively, a cooling rate $\dot{T}$ during L-DED ~3.6×10^{-1} K·s^{-1} is estimated. This value is approximately one order of magnitude higher than that of conventional casting (~4.2×10^{-2} K·s^{-1}), yet remains several orders of magnitude lower than those typically associated with other AM techniques such as L-PBF (~10^2 - 10^4 K·s^{-1}) [17].

Notably, a distinctive tree-ring-like microstructure is observed within individual primary dendrites. On the XY section (Fig. 1d), this structure manifests as concentric rings confined to single dendrite, with the inter-ring spacing progressively decreasing from the dendrite center toward the periphery. On the longitudinal XZ and YZ sections (Fig. 1c), these rings appear as vertical bands aligned with the dendritic growth direction, reflecting a 3D cylindrical ring (or shell) morphology. High-magnification SEM (Fig. 1e) reveals that the rings are composed of locally coarsened γ' precipitates (~402 ± 21 nm), which are significantly larger than those in the region between adjacent rings (299 ± 22 nm).

Elemental mapping and line scans, performed using EPMA (Fig. 2) reveal continuous but pronounced compositional gradient across the dendritic structure. Ti and Nb exhibit a progressive enrichment from DCs toward IRs, whereas W displays the inverse trend. This segregation behavior stems from solidification, where solutes with partition coefficients $k < 1$ (e.g., Ti and Nb) are continuously rejected from the growing solid (i.e., DCs) into the residual liquid [18,19]. As shown in Fig. S3, L-DED generates an ultra-large melt pool (width: 4.2 mm, height: 0.7 mm). Under equivalent heat dissipation conditions, its enhanced thermal capacity prolongs solidification and reduces both the cooling rate and solid–liquid interface propagation rate. Slow solidification provides sufficient time for diffusion of the segregation-prone elements such as Nb and Ti, which are rejected into interdendritic regions at the solidification front. Consequently, a pronounced gradient from IRs to DCs in the γ′ solvus temperature develops (Fig. 2b), consistent with the spatial distribution of Ti. Although elemental segregation is also detected along the tree-ring-like microstructure (Fig. 2c), the magnitude of the concentration variation, in contrast, is considerably smaller.

To elucidate the correlation between the tree-ring-like microstructure and thermomechanical cycling that the solidified alloy experiences during L-DED, microstructures at different heights of the build are examined (Fig. 3). Layers closer to the deposit surface experience fewer thermomechanical cycles, whereas layers at a certain depth below the surface undergo the maximum number of thermal cycles, which remains approximately constant for a given set of AM processing parameters. EBSD and OM observations reveal the following distinct morphological transition (Fig. 3a–c): while the bulk region is dominated by [001]-aligned columnar grains, the top ~1.5 mm region comprises randomly oriented near-equiaxed grains, which primarily arise from altered solidification conditions [20]. Direct exposure to the shielding atmosphere enhances heat extraction, reduces the thermal gradient, and disrupts the directionality of heat flow, thereby promoting a columnar-to-equiaxed transition at the final layer [21].

Beneath the topmost equiaxed region, columnar grains with directional dendrites dominate. Higher magnification SEM indicates that the columnar-grain region can be further subdivided into three distinct zones. Zone I (~1.5 - 7.0 mm below the top surface) is characterized by the complete absence of tree-ring-like microstructure (Fig. 3d). In transitional Zone II (~7.0 - 8.0 mm), the tree-ring-like microstructure begins to emerge, initially manifesting as partial outer rings located near the dendrite periphery (Fig. 3e). In Zone III (≥ 8.0 mm), the concentric patterns become fully developed and well-defined (Fig. 3f). More details about the gradual evolution of the tree-ring-like microstructure along the build direction are provided in Fig. S4. Concurrently, the size of γ′-precipitates increases progressively with increasing distance from the top surface, from 102 ± 9 nm in Zone I to 203 ± 13 nm in Zone III for DCs (details in Fig. S5), evidencing a cumulative thermal aging effect induced by repeated thermal cycles during deposition. It is worth noting that the elemental segregation profile in Zone I (without tree-ring-like microstructure, as shown in Fig. S6) remains similar to that in Zone III (Fig. 2a1–2a4), characterized by Ti and Nb enrichment in IRs and W enrichment in DCs. This confirms that while compositional segregation is a prerequisite, the formation of the rings is strictly triggered by the unique thermal history experienced by the solidified alloy. Notably, calculations using JMatPro (Fig. S6) indicates that the γ' solvus temperature range in Zone I (~90 °C) is about 20 °C wider than that in Zone II (~70 °C).

TEM characterization on the YZ section reveals pronounced differences in the dislocation distributions. In Zone I that is ring-free, IRs

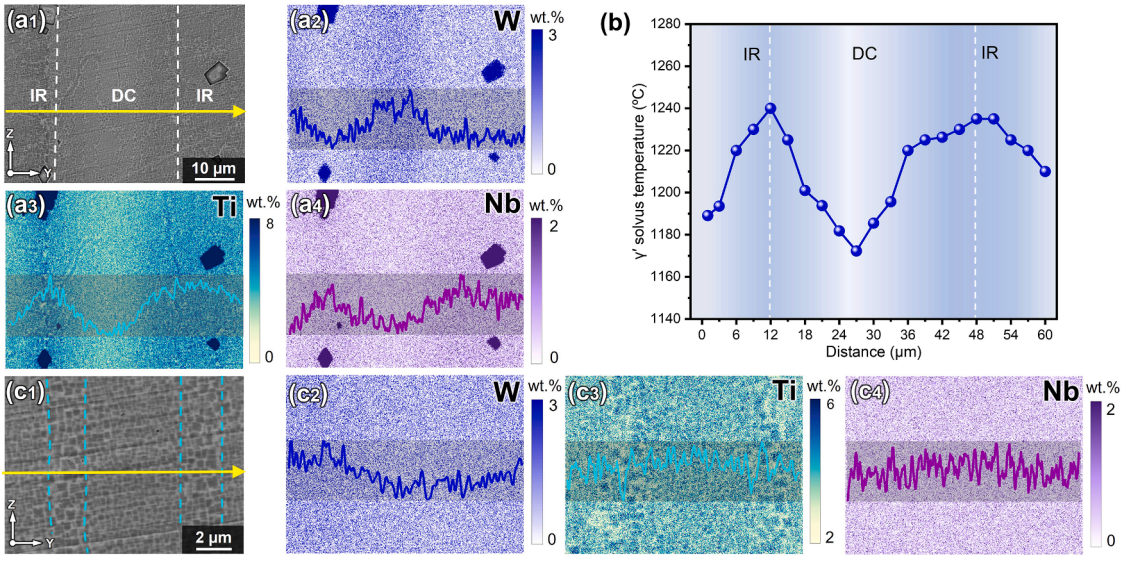


Fig. 2. (a1–a4) EPMA results of the YZ-section of the region cross the dendrites. (b) γ' solvus temperature variation calculated by JMatPro based on the compositional changes along the yellow arrow in (a1). (c1–c4) EPMA results cross the tree-ring-like microstructure within an individual dendrite.

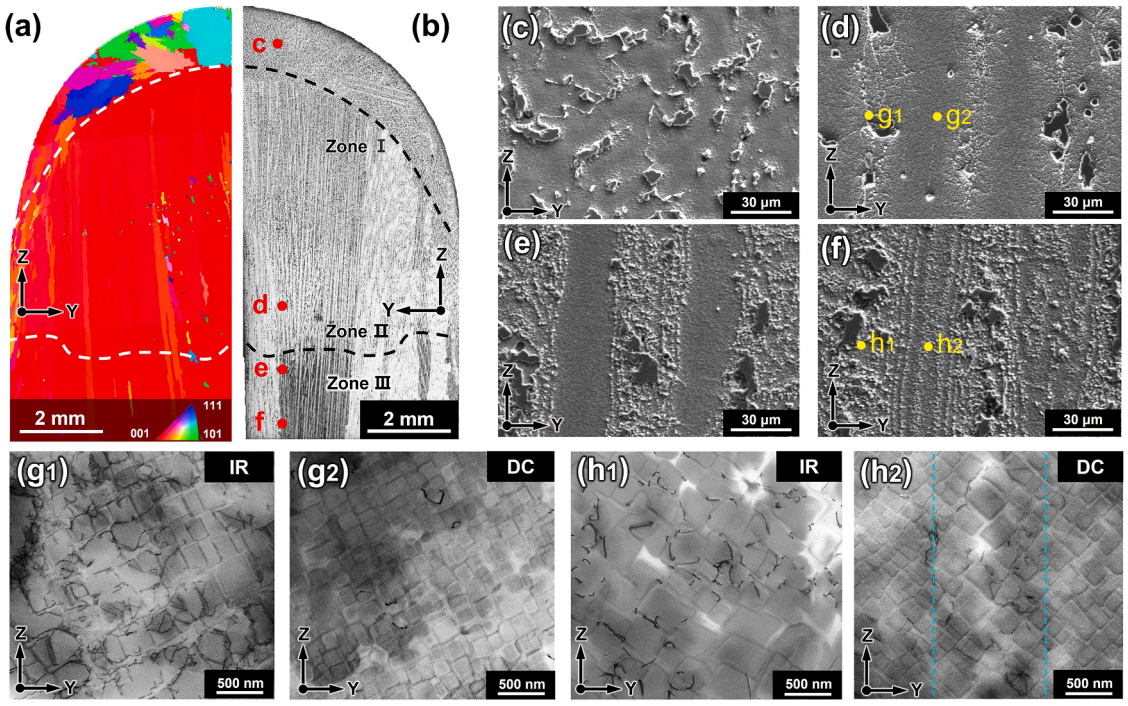


Fig. 3. (a) Grain orientation map with IPF-Z coloring of the YZ-section in the top region; (b) OM image of the same position as (a); (c–d) SEM images at the marked positions in (b); (g1, g2) TEM images at the marked positions in (d); (h1, h2) TEM images at the marked positions in (f).

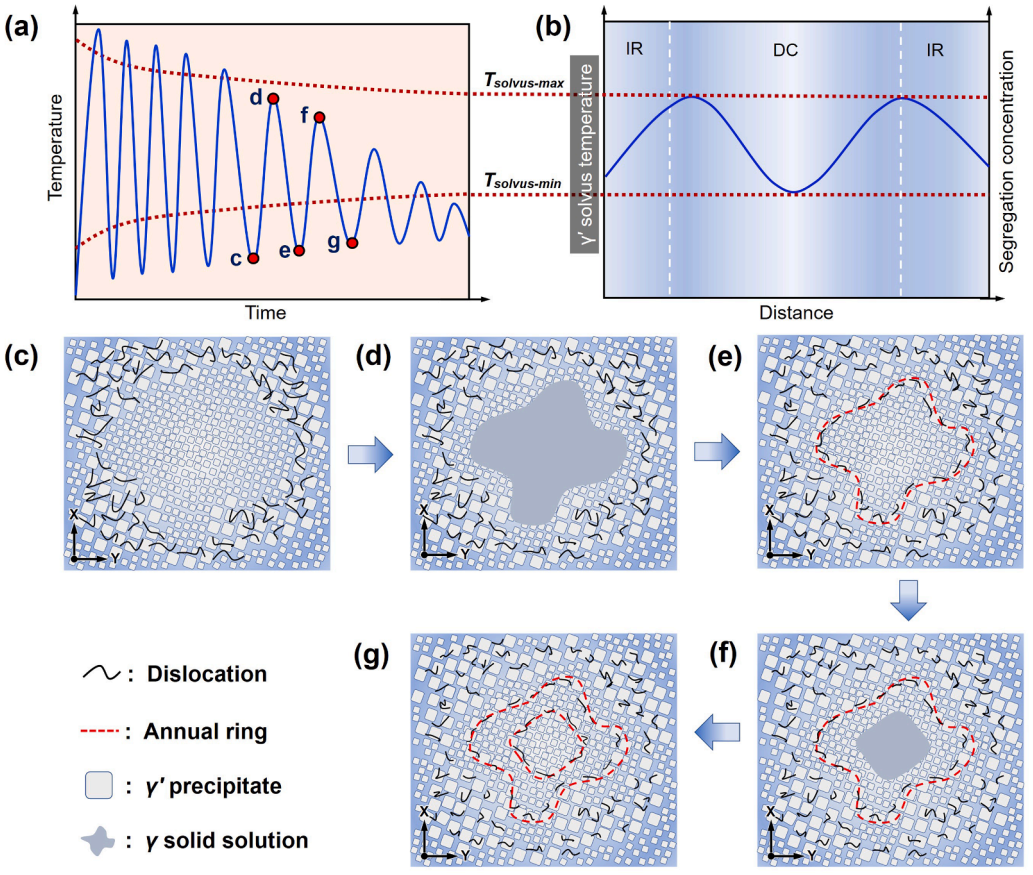


Fig. 4. Schematic diagram of concentric tree-ring-like microstructure formation process: (a) Thermal cycle schematic in the L-DED process; (b) Segregation concentration and γ′ solvus temperature variations within a single dendrite; (c–g) Schematic diagrams of microstructures at red - marked positions.

exhibit a higher dislocation density (Fig. 3g1, 5.1 × 10^{13} m^{-2}) whereas DCs remain relatively dislocation-free (Fig. 3g2, 3.7 × 10^{10} m^{-2}). In

contrast, the distribution of dislocations in Zone III with ring-like features is markedly distinct: the dislocation density in IRs decreases by nearly one order of magnitude (Fig. 3h1, 7.0×10^{12} m^{-2}). Within the DCs, dislocations are no longer statistically random but preferentially pile up along the concentric rings (8.6×10^{11} m^{-2}; blue dashed lines in Fig. 3h2), leaving the inter-ring regions largely dislocation-free. The features observed on the XY section are consistent with this (Fig. S7). These results indicate that cyclic thermal exposure during L-DED not only induces localized phase coarsening, characterized as coarsened γ′ along the rings, but also promotes dynamic recovery, leading to an overall reduction in dislocation density and spatial redistribution of dislocations [22].

On the basis of above observations, we propose the following mechanism for the formation of the tree-ring-like microstructure, which is schematically illustrated in Fig. 4. It is driven by a critical coupling between the cyclic thermal history characteristic of L-DED superalloy and inherent elemental microsegregation. As evidenced in Figs. 2 and S5, pronounced compositional gradients develop from DCs to IRs, arising from the differential partitioning of various solutes (e.g., Ti and W). This segregation establishes a spatially continuous gradient in the γ′ solvus temperature (T_{solvus}) across the dendrite, as confirmed by JMatPro calculations (Fig. 2b), thereby rendering different regions thermodynamically distinct.

During the L-DED process, a fundamental distinction exists between the active melt pool and the underlying material. While the top layers undergo melting, the previously deposited layers primarily experience solid-state phase transformations [23]. Consider a representative solidified dendrite at a given Layer B (Fig. 4c). Deposition of the immediately adjacent layer generates a temperature gradient that decreases from the melting point at the melt pool/solid interface to the bulk. As a result, the peak temperature at Layer B is likely to exceed the upper bound of the solvus temperature ($T_{solvus\text{-max}}$), resulting in the complete dissolution of γ′ precipitates. In this solid solution state, atomic diffusion reduces chemical inhomogeneity and narrows the T_{solvus} range, but does not contribute to the formation of the tree-ring-like microstructure. In the present study, the top portion of the build (approximately 10 mm) is ring-free. Given a melt pool depth of ~0.7 mm (Fig. S3) and a layer increment of 0.3 mm, this suggests that thermal peaks generated by roughly 30 subsequent layers exceed $T_{solvus\text{-max}}$.

As deposition proceeds, the distance between Layer B and the melt pool increases, and the peak temperature at Layer B progressively decreases. After deposition of several layers, the peak temperature falls between $T_{solvus\text{-max}}$ and $T_{solvus\text{-min}}$, resulting in complete dissolution of γ′ in DCs but only partial dissolution in IRs, following the thermal path *c*→*d* in Fig. 4c–e [24]. This behavior arises from spatially heterogeneous elemental segregation, where solutes such as Ti and Nb exhibit strong gradients from DCs to IRs, leading to a corresponding gradient in local T_{solvus} (Fig. 4b). Subsequent cooling produces supersaturation and drives γ′ re-precipitation (from Fig. 4d to 4e).

Concurrently, elevated temperatures of the thermal cycles promote dynamic recovery, reducing dislocation density (from 5.1×10^{13} to 7.0×10^{12} m^{-2}), particularly in regions where γ′ has fully dissolved (Fig. 3h1). In addition, the thermal expansion mismatch between regions with re-precipitated γ′ and those retaining original γ′ generates cyclic thermal stresses during repeated heating and cooling [25,26]. These stresses drive dislocation generation, motion, and localization, often pinned by partially dissolved γ′ particles, leading to preferential dislocation accumulation near the boundaries of partially transformed regions (Fig. 3h2). Acting as diffusion pathways, these dislocations accelerate local γ′ coarsening and lead to the formation of the first concentric ring (Fig. 4e), consistent with previous reports on dislocation-assisted γ′ growth [27].

With increasing build height, the thermal history at Layer B evolves, as the peak temperatures gradually attenuate while the number of thermal cycles accumulates (Fig. 4a). Consequently, the radial position of the isotherm exceeding T_{s_olvus}, as well as the concentric rings, progressively shifts toward the dendrite center. This mechanism is consistent with the microstructural evolution observed along the build direction (Fig. 3), where the ring pattern develops inward from the dendrite periphery with increasing thermal exposure. Therefore, the periodicity of the concentric rings is governed by the combined effects of segregation-induced T_{s_olvus} gradients and cyclic thermal history. The resulting concentric architecture, to some extent, records the transient thermal history of L-DED through segregation-enabled phase transformations.

It is worth noting that while thermomechanical cycling of the solidified alloys is a common feature to many AM techniques, the tree-ring-like microstructure is not commonly observed in AM-processed superalloys, primarily due to the absence of a sufficiently pronounced gradient in γ′ solvus temperature (or the significant elemental segregation). In this work, the specific processing regime, characterized by a larger laser spot size (~3 mm) and high-power input (2500 W), induces the formation of large melt pools (Fig. S3) and facilitates pronounced dendritic microsegregation (e.g., Ti/Nb enrichment in IRs vs. W in DCs), creating the thermodynamic landscape essential for the ring formation. Slight variations in the L-DED parameters still result in the formation of the rings (Fig. S8a). The L-DED processing parameters used in this study are effective in producing tree-ring-like microstructures across multiple Ni-based superalloy compositions and are not restricted to the alloy examined here (Fig. S8a). For instance, modifying the powder composition to 9.0 Cr, 10.0 Co, 3.0 Mo, 5.3 Al, 4.4 Ti, 0.18 C, and 0.018 B, with Ni as the balance (wt %, listed in Table S1), also results in the formation of comparable tree-ring-like microstructures (Fig. S8b). In contrast, distinctly different L-DED processing parameters (beam spot 1.2 mm, power 900 W, scanning speed 20 mm/s, layer thickness 1.5 mm) result in a significantly increased cooling rate and much finer dendrites, and no concentric features are observed in the builds (Fig. S8c).

The tree-ring-like microstructure is not expected to significantly affect strength, as coarsened γ′ particles reduce strength while dislocation accumulation along the concentric walls provides strengthening, leading to a near balance. The concentric microstructure may have a more pronounced influence on high-temperature and long-term mechanical behavior [28]. For example, creep resistance and creep rupture life at elevated temperatures may be affected, as they are governed by γ/γ′ stability, dislocation climb, and diffusion-assisted strain localization. In addition, the ring walls may act as preferential sites for strain localization, thereby promoting the initiation of fatigue damage. We intend to examine these aspects in future.

In summary, a unique tree-ring-like microstructure is observed in an L-DED fabricated Ni-based superalloy. Its formation mechanism is governed by the coupling of two prerequisites: a segregation-induced γ' solvus gradient and thermal cycling of the solidified alloy. This is evidenced by the absence of rings in the topmost layers and the progressive increase in ring numbers with build height. Although thermal cycling is inherent to AM, such tree-ring-like microstructure are not observed in other studies mainly due to the lack of a sufficiently pronounced solvus gradient, underscoring the essential role of severe elemental segregation. Mechanistically, the structure evolves only in regions experiencing sufficient thermal cycles, arising from repeated γ ⇌ γ′ transformations, dislocation redistribution, and concurrent dynamic recovery. Together, these processes imprint the transient thermal history of L-DED into a distinctive concentric microstructural morphology.

CRediT authorship contribution statement

Yang Wang: Writing – original draft, Investigation, Data curation. **Zhaowei Wang:** Validation, Methodology, Investigation. **Sicong Lin:** Resources. **Zhuangzhuang Zhang:** Validation. **Lin Shi:** Visualization. **Qiang Li:** Writing – review & editing, Visualization. **R. Lakshmi Narayan:** Writing – review & editing. **Upadrasta Ramamurty:** Writing – review & editing. **Kai Chen:** Writing – review & editing, Supervision, Funding acquisition, Conceptualization.

Declaration of competing interest

The authors declare that they have no known competing financial interests or personal relationships that could have appeared to influence the work reported in this paper.

The author Upadrasta Ramamurty is an Editor for Scripta Materialia, and was not involved in the editorial review or the decision to publish this article.

Acknowledgements

This work is supported by the open research fund of Suzhou Laboratory no SZLAB-1608-2025-TS040, the National Key Research and Development Program of China under grant 2023YFB12002, and the National Natural Science Foundation of China (grant no W2411048, 22409160). We also thank Instrumental Analysis Center of Xi'an Jiaotong University and Dr. Chuanwei Fan for technical support.

Supplementary materials

Supplementary material associated with this article can be found, in the online version, at doi:10.1016/j.scriptamat.2026.117392.

References

[1] Z. Wang, F. Liu, S. Gao, Q. Li, K. Chen, Turn nonweldable Ni-superalloys printable and microstructurally controllable, Adv. Mater. (2026) e17003.
[2] L. Kovarik, R.R. Unocic, J. Li, P. Sarosi, C. Shen, Y. Wang, et al., Microtwinning and other shearing mechanisms at intermediate temperatures in Ni-based superalloys, Prog. Mater Sci. 54 (6) (2009) 839–873.
[3] K. Chen, R. Huang, Y. Li, S. Lin, W. Zhu, N. Tamura, et al., Rafting-enabled recovery avoids recrystallization in 3D-printing-repaired single-crystal superalloys, Adv. Mater. 32 (12) (2020) 1907164.
[4] Z. Sun, W. Guo, L. Li, Numerical modelling of heat transfer, mass transport and microstructure formation in a high deposition rate laser directed energy deposition process, Addit. Manuf. 33 (2020) 101175.
[5] Z. Li, S. Sui, X. Ma, H. Tan, C. Zhong, G. Bi, et al., High deposition rate powder- and wire-based laser directed energy deposition of metallic materials: a review, Int. J. Mach. Tools Manuf. 181 (2022) 103942.
[6] C. Ren, K. Chen, J. Liang, R.L. Narayan, U. Ramamurty, J. Li, Microstructural evolution and its influence on the wear resistance of a laser directed energy deposited Ni-based single crystal superalloy, J. Mater. Sci. Technol. 205 (2025) 127–138.
[7] X. Wang, K. Chou, Effects of thermal cycles on the microstructure evolution of Inconel 718 during selective laser melting process, Addit. Manuf. 18 (2017) 1–14.
[8] X. Zou, Z. Yan, K. Zou, W. Liu, L. Song, S. Li, et al., Grain refinement by dynamic recrystallization during laser direct energy deposition of 316L stainless steel under thermal cycles, J. Manuf. Process. 76 (2022) 646–655.
[9] H. Zhang, K. Chen, W. Pantleon, H. Shen, E. Ma, High-temperature deformation of Ni-based superalloy and recrystallization prevention by recovery, Scr. Mater. 265 (2025) 116732.
[10] Y. Li, K. Chen, R.L. Narayan, U. Ramamurty, Y. Wang, J. Long, et al., Multi-scale microstructural investigation of a laser 3D printed Ni-based superalloy, Addit. Manuf. 34 (2020) 101220.
[11] S. Chandra, J. Radhakrishnan, S. Huang, S. Wei, U. Ramamurty, Solidification in metal additive manufacturing: challenges, solutions, and opportunities, Prog. Mater Sci. 148 (2025) 101361.
[12] H. Yu, Z. Wang, B. Zhang, Y. Ning, M.W. Fu, Re-precipitation mechanisms of the γ′ phase with sphere, near-sphere, cubic, octets and finally-dendrite in as-cast Ni-based superalloys, J. Alloy. Compd. 876 (2021) 160104.
[13] Y. Tian, J.A. Muñiz-Lerma, M. Brochu, Nickel-based superalloy microstructure obtained by pulsed laser powder bed fusion, Mater. Charact. 131 (2017) 306–315.
[14] V.K. Singh, D. Sahoo, A. Ranjan, M. Amirthalingam, S. Karagadde, S.K. Mishra, Comparison of tensile and LCF behaviour of heat-treated Inconel 718 printed by LPBF and LW-DED at different temperatures, Int. J. Fatig. 198 (2025) 109010.
[15] D. Wu, Z. Zhang, Z. Guo, D. Hu, Z. Wang, W. Wu, et al., Analysis of the intermediate temperature brittleness of LPBF-fabricated Ni-based alloys with high γ′ phase fraction, Mater. Sci. Eng. A 953 (2026) 149713.
[16] Y. Zhao, Z. Wang, L. Shi, S. Gao, D. Qian, K. Chen, et al., Simultaneous strength optimization and recrystallization prevention in induction-heating-assisted laser additively manufactured Ni-based superalloys, Mater. Res. Lett. 13 (6) (2025) 632–641.
[17] T. DebRoy, H.L. Wei, J.S. Zuback, T. Mukherjee, J.W. Elmer, J.O. Milewski, et al., Additive manufacturing of metallic components – process, structure and properties, Prog. Mater Sci. 92 (2018) 112–224.
[18] F. Wang, D. Ma, A. Bührig-Polaczek, Microsegregation behavior of alloying elements in single-crystal nickel-based superalloys with emphasis on dendritic structure, Mater. Charact. 127 (2017) 311–316.
[19] N. Ren, C. Panwisawas, J. Li, M. Xia, H. Dong, J. Li, Solute enrichment induced dendritic fragmentation in directional solidification of nickel-based superalloys, Acta Mater. 215 (2021) 117043.
[20] J. Nie, C. Chen, L. Liu, X. Wang, R. Zhao, S. Shuai, et al., Effect of substrate cooling on the epitaxial growth of Ni-based single-crystal superalloy fabricated by direct energy deposition, J. Mater. Sci. Technol. 62 (2021) 148–161.
[21] T.D. Anderson, J.N. DuPont, T. DebRoy, Origin of stray grain formation in single-crystal superalloy weld pools from heat transfer and fluid flow modeling, Acta Mater. 58 (4) (2010) 1441–1454.
[22] H. Zhang, K. Chen, S. Lin, R. Fu, B. Zhang, J. Ding, et al., Recovery facilitated by interphase boundary motion circumvents recrystallization in superalloy single crystals, Mater. Res. Lett. 12 (3) (2024) 180–189.
[23] V. Manvatkar, A. De, T. DebRoy, Heat transfer and material flow during laser assisted multi-layer additive manufacturing, J. Appl. Phys. 116 (12) (2014) 124905.
[24] S. Lin, K. Chen, W. He, N. Tamura, E. Ma, Custom-designed heat treatment simultaneously resolves multiple challenges facing 3D-printed single-crystal superalloys, Mater. Des. 222 (2022) 111075.
[25] R.J. Moat, A.J. Pinkerton, L. Li, P.J. Withers, M. Preuss, Residual stresses in laser direct metal deposited Waspaloy, Mater. Sci. Eng. A 528 (6) (2011) 2288–2298.
[26] X. Song, S. Feih, W. Zhai, C.-N. Sun, F. Li, R. Maiti, et al., Advances in additive manufacturing process simulation: residual stresses and distortion predictions in complex metallic components, Mater. Des. 193 (2020) 108779.
[27] T.M. Smith, Y. Rao, Y. Wang, M. Ghazisaeidi, M.J. Mills, Diffusion processes during creep at intermediate temperatures in a Ni-based superalloy, Acta Mater. 141 (2017) 261–272.
[28] S.-H. Li, Y. Zhao, P. Kumar, U. Ramamurty, Effect of initial dislocation density on the plastic deformation response of 316L stainless steel manufactured by directed energy deposition, Mater. Sci. Eng. A 851 (2022) 143591.